Langevin approach to lattice dynamics in a charge-ordered polaronic system

Sauri Bhattacharyya, Sankha Subhra Bakshi, Samrat Kadge, and Pinaki Majumdar
Harish-Chandra Research Institute, HBNI, Chhatnag Road, Jhusi, Allahabad 211019, India

(Received 4 March 2019; published 30 April 2019)

We use a Langevin approach to treat the finite temperature dynamics of displacement variables in the half-filled spinless Holstein model. Working in the adiabatic regime we exploit the smallness of the adiabatic parameter to simplify the memory effects and estimate displacement costs from an "instantaneous" electronic Hamiltonian. We use a phenomenological damping rate and uncorrelated thermal noise. The low temperature state has checkerboard charge order (CO) and the Langevin scheme generates equilibrium thermodynamic properties that accurately match Monte Carlo results. It additionally yields the dynamical structure factor, $D(\mathbf{q}, \omega)$, from the displacement field $x(\mathbf{r}, t)$. We observe four regimes with increasing temperature T classified in relation to the charge ordering temperature T_c and the 'polaron formation' temperature T_P, with $T_c \ll T_P$. For $T \ll T_c$ the oscillations are harmonic, leading to dispersive phonons, with increasing T bringing in anharmonic, momentum dependent, corrections. For $T \sim T_c$, thermal tunneling events of the $x(\mathbf{r})$ field occur, with a propagating 'domain' pattern at wave vector $\mathbf{q} \sim (\pi, \pi)$ and low energy weight in $D(\mathbf{q}, \omega)$. When $T_c < T < T_P$, the disordered polaron regime, domain structures vanish, the dispersion narrows, and low energy weight is lost. For $T \gtrsim T_P$ we essentially have uncorrelated local oscillations. We propose simple models to analyze the rich dynamics.

DOI: 10.1103/PhysRevB.99.165150

I. INTRODUCTION

Apart from its ubiquitous effect on electronic resistivity [1], electron-phonon (EP) interaction leads to collective states like superconductivity [2] and charge or orbital order [3]. While the physics at weak EP coupling is perturbative, strong EP coupling leads to the formation of an electron-phonon bound state—a small polaron [4]. Residual interaction among the polarons can lead to long range order, but signatures of a polaronic state survive well above any ordering temperature. Experiments on several materials [5–7] over the last couple of decades have established this.

Experiments probe strong coupling EP physics at various levels. The static structural properties that result from EP coupling, including charge ordering, have been characterized in detail [8–10]. The dynamical structure factor associated with lattice fluctuations can be directly probed via inelastic neutron scattering (INS) [11]. The dynamics of the large amplitude lattice displacements feed back on the electron system leading to unusual spectral signatures observable through angle resolved photoemission spectroscopy (ARPES). Such data is already available in the manganites [12]. Beyond equilibrium, several studies have probed the response of EP systems to intense radiation, via 'pump-probe' experiments [13], exploring the exchange of energy between the electron and phonon subsystems and the approach to equilibrium. While static structural properties are well understood, dynamical properties and the physics out of equilibrium remain sparsely explored. Our focus in this paper is on the dynamics at equilibrium.

At weak EP coupling the lattice dynamics is affected via the electronic polarizability—modifying the dispersion and causing damping—and the band susceptibility adequately describes phonon properties [14] over a reasonable temperature range. At strong EP coupling, however, when the electronic state itself is strongly renormalized and temperature dependent, one needs a fully self-consistent treatment of the coupled electron-phonon problem. Amongst the nonperturbative tools available, quantum Monte Carlo (QMC) [15] is numerically exact but subject to sign problems, large computation cost, and difficulty in extracting real frequency information. Dynamical mean field theory (DMFT) [16] avoids the size dependence by exploring a self-consistent impurity problem but ignores spatial correlations which are important near the thermal transition.

There are several puzzling issues that remain only partially understood in phonon dynamics. These include: (i) the relation between the anomalous softening and broadening of phonons and short range charge-orbital order [17–19], (ii) spatiotemporal fluctuations near an ordering transition, and (iii) the relaxation from a 'nonequilibrium' initial state, created, for instance, by intense radiation, to a thermal distribution.

Theoretical studies until now focus either on one dimension—addressing physics near the Peierls transition [20,21] and at dilute filling [22]—or within DMFT [23,24]. The phonon softening feature at the zone boundary near the Peierls transition has been revealed by multiple approaches before [25–27]. However, none of these focus on finite temperature phonon dynamics. To approach issues (i)–(iii) above we need a method that (a) handles strong EP coupling, spatial correlations, and thermal fluctuations, (b) yields real time dynamics, and, hopefully, (c) handles nonequilibrium situations.

A systematic approach to this problem requires the Keldysh framework [28]. We will show in the paper how a tractable scheme can be derived from the Keldysh starting point by assuming smallness of the 'adiabatic parameter,' i.e., the ratio of bare phonon and electron energy scales, and a high temperature approximation for the 'noise' that acts on the

phonon variables. With these assumptions, and a microscopically motivated choice of phonon damping, γ, a Langevin equation [29–31] can be written for the displacement field. The equation that emerges has a parallel in classical many body physics, in particular the study of dynamical critical phenomena [32]. The approach has also seen recent use in the study of spin dynamics in the Hubbard model [33].

In this paper we use the Langevin dynamics (LD) approach to study the half-filled spinless Holstein model in two dimensions and intermediate coupling. Our focus is on the dynamical signatures as the temperature is increased through the charge ordering transition at T_c into the 'polaron liquid' phase. The charge order (CO) is at wave vector $\mathbf{Q} = (\pi, \pi)$. We benchmarked the LD based charge ordering results against Monte Carlo (MC) and found excellent agreement. We focus on the dynamical structure factors, $D_{nn}(\mathbf{q}, \omega)$ and $D_{xx}(\mathbf{q}, \omega)$, which are, respectively, the Fourier transforms of the correlation function $\langle n_{\mathbf{r}}(t) n_{\mathbf{r}'}(t')\rangle$ and $\langle x_{\mathbf{r}}(t) x_{\mathbf{r}'}(t')\rangle$, $n_{\mathbf{r}}$ being the electron density and $x_{\mathbf{r}}$ the phonon displacement. Most of our results show $D_{xx}(\mathbf{q}, \omega)$ which we directly compute as $|X(\mathbf{q}, \omega)|^2$, where $X(\mathbf{q}, \omega)$ is the Fourier transform of the displacement field $x(\mathbf{r}, t)$. We measure time in units of τ_0, the bare oscillation period for the local phonons. Our key results are the following:

(1) For $T \ll T_c$ we observe dispersive phonons with frequency $\omega_{\mathbf{q}}$ that can be understood within a harmonic nearest neighbor model. The damping $\Gamma_{\mathbf{q}}$ is dictated by γ and is momentum independent. Increasing T leads to anharmonic signatures—$\mathbf{q}$ dependent softening of $\omega_{\mathbf{q}}$ and increase of $\Gamma_{\mathbf{q}}$. Both these changes, $\delta\omega_{\mathbf{q}}$ and $\delta\Gamma_{\mathbf{q}}$, are proportional to T to leading order.

(2) As T approaches T_c we observe three effects—(a) occasional large displacements at some site, with a quick reversal to the original state, (b) near T_c, a spatially correlated oscillatory pattern of large displacements mimicking 'domain growth,' and (c) oscillations with large period, $\gtrsim 100\tau_0$, generate huge low energy weight in $D(\mathbf{q} \sim \mathbf{Q}, \omega)$, leading to a dramatic softening of the dispersion and reduction of the damping.

(3) In the polaron liquid phase, $T_c < T < T_P$, short range correlated polaronic distortions persist (over a window up to $\sim 10T_c$ in our case). The low energy feature in $D(\mathbf{q}, \omega)$ is gradually lost and the dispersion narrows. We also see a quick reduction in phonon linewidths. The dispersion is undetectable for $T \gtrsim 10T_c \sim T_P$.

II. MODEL AND METHOD

A. Hamiltonian and parameter space

We study the single band, spinless, Holstein model on a 2D square lattice:

$$H = \sum_{ij}(t_{ij} - \mu\delta_{ij})c_i^\dagger c_j + \sum_i \left(\frac{p_i^2}{2M} + \frac{1}{2}Kx_i^2\right) - g\sum_i n_i x_i. \quad (1)$$

Here, t_{ij}'s are the hopping amplitudes. We study a nearest neighbor model with $t = 1$ at $n = 0.5$ (half filling). K and M are the stiffness constant and mass, respectively, of the optical phonons, and g is the electron-phonon coupling constant. We set $K = 1$. In this paper, we report studies for $\Omega = \sqrt{K/M} = 0.1$, which is a reasonable value for real materials. We focus on a fixed, intermediate coupling value $g = 2.0$. The chemical potential μ is set so that $n = 0.5$.

B. Keldysh to Langevin

The Holstein problem can be set up in the Keldysh language in terms of coherent state fields corresponding to x_i and c_i operators, with their full space-time dependence retained. We will indicate how a Langevin-like equation of motion can be obtained from the Keldysh action in the adiabatic limit. Physically, taking this limit corresponds to a "small $\dot{x}$" approximation, namely the velocity of this field is assumed to be much smaller than Fermi velocity. We outline this below.

The partition function for the x_i 'oscillators' can be written as

$$Z_{\text{osc}} = \int Dx_{i,f} Dx_{i,r} e^{i(S_0 + S_1)}. \quad (2)$$

Here $x_{i,f}$ and $x_{i,r}$ are lattice displacement fields along the forward and return contours, respectively. The expressions for S_0 and S_1 are

$$S_0 = \frac{1}{2}\int dt \left[\sum_i (M\ddot{x}_{i,f} + Kx_{i,f})x_{i,f} - (M\ddot{x}_{i,r} + Kx_{i,r})x_{i,r}\right]$$
$$S_1 = iTr(\log([\mathcal{G}^{-1}]_{ij}(t, t')), \quad (3)$$

where $\mathcal{G}$ is the matrix electron Green's function (with $N \times N$ dimension in real space and 2×2 in Keldysh space) in a time fluctuating $(x_{i,f}, x_{i,r})$ 'background.'

To facilitate the derivation, one can transform to new 'classical' and 'quantum' variables $x_{i,cl} = \frac{x_{i,f} + x_{i,r}}{2}$, $x_{i,q} = x_{i,f} - x_{i,r}$. The next important step is to assume the characteristic oscillator frequency Ω to be much smaller than the electronic energy scales (nominally the hopping t in our model). We can now perturbatively expand S_1 in powers of $x_{i,q}(t)$ while retaining $x_{i,cl}(t)$ nonperturbatively in the theory. The parameter that controls the expansion [29] is Ω/t. Physically, the expansion in powers of $x_{i,q}(t)$ means we're adopting a semiclassical picture. Expanding up to linear order gives classical deterministic phonon dynamics. The quadratic term carries the effect of an added noise. This is done following the lines of Ref. [29]. The look of the effective action now is

$$S_{\text{eff}} = S_0 + g\sum_i \int dt \left[G^K_{cl}\right]_{ii}(t, t)x_{i,q}(t) + g^2 \sum_{ij}\int dt dt' \left[\Pi^K_{cl}\right]_{ij}(t, t')x_{i,q}(t)x_{j,q}(t'),$$

where $[G^K_{cl}]$ is the Keldysh component of electron Green's function $\mathcal{G}$ computed setting $x_{i,q} = 0$. The quantity $[\Pi^K_{cl}]$ is the Keldysh component of electronic polarizability for $x_{i,q} = 0$, related to the Green's functions by the relation

$$\Pi^K_{ij}(t, t') = G^R_{ij}(t, t')G^A_{ji}(t', t) + (R \leftrightarrow A) + G^K_{ij}(t, t')G^K_{ji}(t', t)$$

G^R and G^A being retarded and advanced components of $\mathcal{G}$.

The coefficients of the linear and quadratic terms in $x_{i,q}(t)$ are thus determined through computing electronic correlation functions in an 'arbitrary' $x_{i,cl}(t)$ background. This calculation can be simplified by expanding the 'trajectories' $x_{i,cl}(t)$ around a reference time t_0 in powers of the velocity $\dot{x}_{i,cl}$. The velocity independent term is interpreted in terms of a force exerted by an instantaneous effective Hamiltonian. The linear in $\dot{x}_{i,cl}$ term gives rise to 'damping' with a frequency dependent kernel.

The next stage of approximation concerns the frequency dependence of the Keldysh component of electronic polarizability $\Pi^K_{ij}(\omega)$. At equilibrium, the frequency dependence of this quantity can be factored according to fluctuation-dissipation theorem [28] as

$$\Pi^K_{ij}(\omega) = coth\left(\frac{\omega}{2k_BT}\right)\left(\Pi^R_{ij}(\omega) - \Pi^A_{ij}(\omega)\right), \tag{4}$$

where Π^R_{ij} and Π^A_{ij} are the retarded and advanced components of the polarizability, respectively. These are defined as

$$\Pi^{R/A}_{ij}(t,t') = G^{R/A}_{ij}(t,t')G^K_{ji}(t',t) + (R/A \leftrightarrow K). \tag{5}$$

Next, we make the high temperature ($k_BT \gg \omega$) approximation on the RHS. The hyperbolic cotangent gives a factor of $(2k_BT/\omega)$, and the low frequency spectral part of Π contributes $\gamma\omega$, where $\gamma = g^2\frac{Im(\Pi^R(\omega))}{\omega}$ and we've neglected the spatial dependence of the polarizability.

If one carefully carries out the evaluation of the linear in velocity ($\dot{x}_{i,cl}$) term, the coefficient comes out to be the spectral part of the polarizability $Im(\Pi^R_{ij}(\omega))$. Again neglecting spatial dependences here and taking the low-frequency limit, the term simplifies to $\gamma\omega$ and becomes the usual nonretarded Langevin damping coefficient.

Finally, one decouples the quadratic term in $x_{i,q}(t)$ through a Hubbard-Stratonovich transformation introducing a 'noise' field $\xi_i(t)$ and then integrates over $x_{i,q}(t)$ in the partition function to obtain an 'equation of motion' [28] for $x_{i,cl}(t)$. This leads to our dynamical equation, below.

C. Effective equation

The dynamical equation which we solve for the phonon field is the following

$$\begin{aligned}
M\ddot{x}_i(t) &= -\gamma\dot{x}_i(t) - Kx_i(t) - \frac{\partial\langle H_{el}\{x\}\rangle}{\partial x_i} + \xi_i(t)\\
H_{el} &= \sum_{ij}(t_{ij} - \mu\delta_{ij})c^\dagger_i c_j - g\sum_i n_i x_i\\
\frac{\partial\langle H_{el}\{x\}\rangle}{\partial x_i} &= -g\bar{n}_i(t)\\
\bar{n}_i(t) &= \sum_{\epsilon_n(t)}|U_{in}(t)|^2 n_f(\epsilon_n(t)),
\end{aligned} \tag{6}$$

where $U_{in}(t)$ are site amplitudes of the instantaneous eigenvectors of H [as in Eq. (1)] for a given $x_i(t)$ configuration and $\epsilon_n(t)$ are the corresponding eigenvalues. $n_f(\epsilon_n(t))$ denotes Fermi factors needed to calculate the instantaneous density field. Note that the spatial correlations in this arise only via the dependence of the density $\bar{n}_i$ on the field $\{x_i\}$.

The first term describes damping, second and third are effective forces, and the last one is the noise field, which is specified by the conditions

$$\begin{aligned}
\langle\xi_i(t)\rangle &= 0\\
\langle\xi_i(t)\xi_j(t')\rangle &= 2\gamma k_BT\delta_{ij}\delta(t-t').
\end{aligned}$$

The unit of time is taken to be the inverse of the bare oscillator frequency $\tau_0 = 2\pi/\Omega$. For most of our simulations, we chose $\gamma = 1.0t$, which sets the damping timescale to $2M/\gamma = 3\tau_0$. The imaginary part of the retarded polarizability $Im\Pi^R(\mathbf{q},\omega)$ is gapped at low T in the present model. At intermediate temperatures, it picks up a low energy contribution proportional to ω. The microscopic estimate of γ, based on $Im\Pi^R$, is smaller and also T dependent. To minimize parameter variation and ensure reasonably rapid equilibration we have set $\gamma = 1$.

We integrate the equation numerically using the well-known Euler-Maruyama method. The time discretization for most calculations was set to $\Delta t = 1.6\times10^{-4}\tau_0$. We typically ran the simulations for $\sim10^7$ steps, ensuring a time span of almost a few hundred times the equilibration time. This ensured enough frequency points to analyze the power spectrum.

D. Indicators

We quantify the equal-time and dynamical properties through several indicators. We first define some timescales. We set an 'equilibration time' $\tau_{eq} = 100\tau_0$ before saving data for the power spectrum. The outer timescale, $\tau_{max} \sim 10\tau_{eq}$. The 'measurement time' $\tau_{meas} = \tau_{max} - \tau_{eq}$, and the number of sites is N. We calculate the following:

(1) Dynamical structure factor, $D(\mathbf{q},\omega) = |X(\mathbf{q},\omega)|^2$, where

$$X(\mathbf{q},\omega) = \sum_{ij}\int_{\tau_{eq}}^{\tau_{max}} dt e^{i\mathbf{q}.(\mathbf{r}_i-\mathbf{r}_j)}e^{i\omega(t-t')}x(\mathbf{r}_i,t)x(\mathbf{r}_j,t').$$

(2) The instantaneous structure factor

$$S(\mathbf{q},t) = \frac{1}{N^2}\sum_{ij} e^{i\mathbf{q}.(\mathbf{r}_i-\mathbf{r}_j)}x(\mathbf{r}_i,t)x(\mathbf{r}_j,t).$$

The instantaneous 'order parameter' is $S(\mathbf{Q},t)$, and the time averaged structure factor is

$$\bar{S}(\mathbf{q}) = \frac{1}{\tau_{meas}}\int_{\tau_{eq}}^{\tau_{max}} dt e^{i\omega t}S(\mathbf{q},t).$$

(3) The distribution of distortions:

$$P(x) = \frac{1}{N\tau_{meas}}\sum_i\int_{\tau_{eq}}^{\tau_{max}} dt\delta(x - x_i(t)).$$

(4) Dispersion $\omega_{\mathbf{q}}$ and damping $\Gamma_{\mathbf{q}}$:

$$\omega_{\mathbf{q}} = \int_0^{\omega_{max}} d\omega\omega D(\mathbf{q},\omega)$$

$$\Gamma^2_{\mathbf{q}} = \int_0^{\omega_{max}} d\omega(\omega-\omega_{\mathbf{q}})^2 D(\mathbf{q},\omega).$$

While calculating moments, we've normalized by $((g/K)^{-2})$, to ensure dimensional consistency.

(5) We show spatial maps for the overlap of $x_i(t)$ with a perfect CO with alternating distortions 0 and g/K.

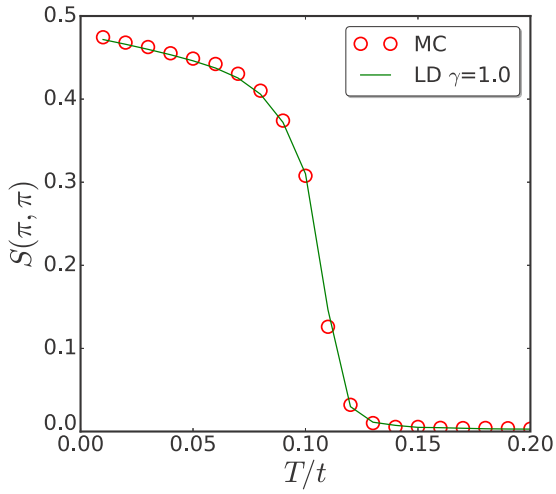

FIG. 1. Comparison of $S(\pi,\pi)$ computed using Langevin dynamics (green line) and MC annealing (red open circles).

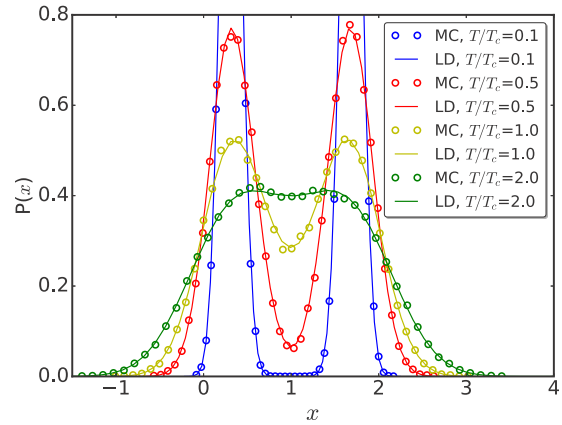

FIG. 2. Comparison of displacement distribution $P(x)$ obtained using Langevin dynamics (solid lines) and MC annealing (open circles) in various temperature regimes.

III. BENCHMARKING WITH MONTE CARLO

In this section we compare the CO order parameter and the distribution $P(x)$ of lattice deformations, obtained via (i) Langevin dynamics and (ii) via Monte Carlo simulation of the adiabatic Holstein model [defined by the $M \to \infty$ limit of Eq. (1).

A. Order parameter

Fig. 1 compares $S(\pi,\pi)$ from Langevin dynamics for various γ values with that from MC annealing (red open circles). The agreement is excellent at $\gamma = 1$, and generally good at the other γ as well. The transition temperature $T_c \sim 0.12t$ is inferred from the onset of rise in both curves. The transition is in the Ising class. However, the low T behavior differs from that of the Ising model due to the continuous nature of the x_i variable. The dependence on γ is weak, but higher γ generally leads to better correspondence with equilibrium MC results.

B. $P(x)$ distributions

In Fig. 2 we show the $P(x)$ obtained from a Monte Carlo calculation, compared to results from LD at $\gamma = 1$. The dynamical method gives histograms quantitatively comparable to the MC results. We plot the distributions at four temperatures: 0, $0.5T_c$, T_c, $2T_c$. The solid lines are the Langevin data whereas open circles depict results from MC annealing. The agreement suggests that the two methods should predict the same 'equal-time' properties in equilibrium.

IV. REAL TIME DYNAMICS

We classify our results into four thermal regimes: (a) low temperature, $T \lesssim 0.6T_c$, where the dynamics is harmonic or mildly anharmonic, (b) the 'critical' window, $0.6T_c \lesssim T \lesssim 1.5T_c$, where thermal tunneling events dominate, (c) the 'polaron liquid' phase, $1.5T_c \lesssim T \lesssim 10T_c \sim T_P$, where the distortions and density still have a bimodal character but spatial correlations are only short range, and (d) the 'polaron dissociated' phase, $T \gtrsim T_P$, where we have essentially independent local oscillations. For each of these regimes we typically show some trajectories for the real space dynamics, time dependence of some Fourier modes, the power spectrum, and sometimes damping and dispersion scales extracted from the power spectrum.

A. Harmonic and weakly anharmonic regime: $T \ll T_c$

1. Real time trajectories

Fig. 3 shows the time dependence of phonon variable both in real and momentum space at $T = 0.1T_c$ and $T = 0.5T_c$.

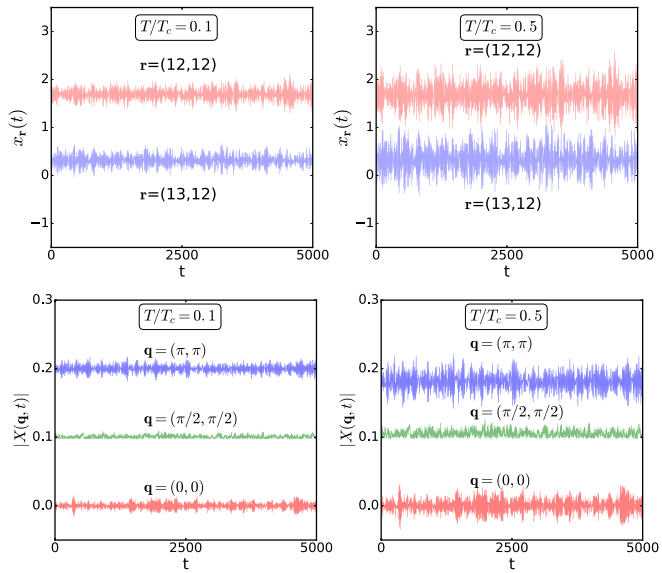

FIG. 3. Top panels: Trajectories of nearest neighbor sites for part of the full time series. We see harmonic vibrations about equilibrium positions in the left figure. The fluctuation window increases considerably on heating ($0.5T_c$), featured in the right figure. Bottom panels: Corresponding Fourier mode trajectories at the same temperatures. The means are subtracted and trajectories shifted by a constant in the left figure ($0.1T_c$). The effect of anharmonicity is to reduce the mean $X(\pi,\pi)$ and visibly enhance fluctuations in both (0,0) and (π,π) modes.

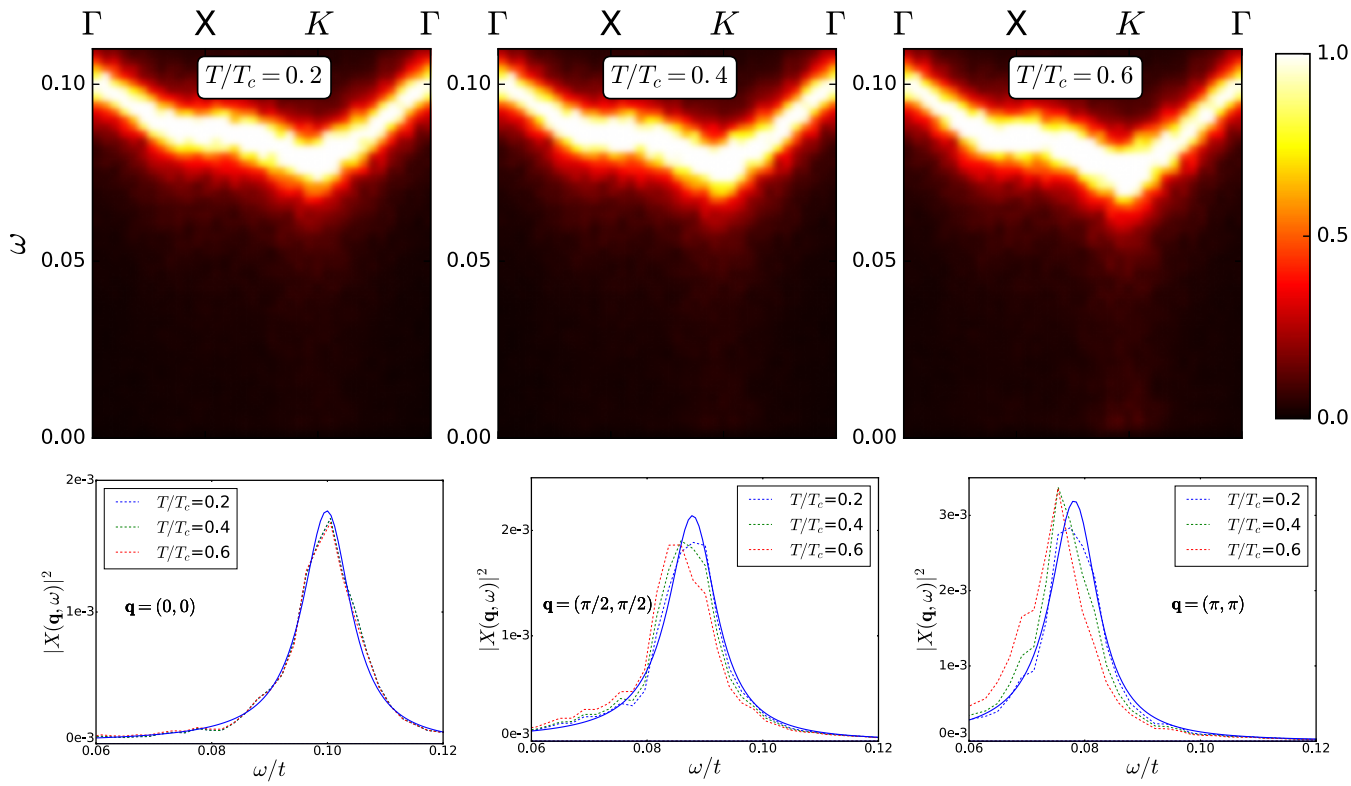

FIG. 4. Top row: False color maps of the power spectrum $|X(\mathbf{q},\omega)|^2$ in the low temperature regime. The spectral intensities are plotted with the momentum trajectory $(0,0) \to (\pi,0) \to (\pi,\pi) \to (0,0)$ along the x-axis. Bottom row: Lineshapes at corresponding temperature points for three momentum points along the BZ diagonal: (0,0), $(\pi/2,\pi/2)$ and (π,π). All power spectra are normalized by k_BT.

The top left panel shows the trajectories $x_{\mathbf{r}}(t)$ at nearest neighbor sites, $\mathbf{r} = (12,12)\&(13,12)$ at $T = 0.1T_c$, while the top right panel shows the same at $T = 0.5T_c$. The $0 < T < 0.6T_c$ window roughly defines the 'low temperature' regime as we discuss below. The left panel shows small amplitude vibrations about mean distortions ~ 0 and 2, respectively. The right panel shows a qualitative increase in fluctuation amplitude, retaining similar mean values.

The bottom panel depicts trajectories $|X(\mathbf{q},t)|$ at three momenta along the Brillouin zone (BZ) diagonal. The left panel is at $T = 0.1T_c$, the right at $T = 0.5T_c$. In the left panel we subtracted the mean values and shifted the curves by a constant (0.1) to aid visualization. The $\mathbf{q} = (0,0)$ and (π,π) modes are seen to fluctuate more compared to $(\pi/2,\pi/2)$. In the right panel the mean $|X(\pi,\pi,t)|$ reduces. Oscillations are most prominent at (π,π).

2. Power spectrum

We turn now to the description of dynamics in terms of $|X(\mathbf{q},\omega)|^2$. The top row of Fig. 4 features the results in the low temperature regime. The maps are color coded in terms of varying intensity and the X axis shows a momentum scan along the trajectory $(0,0) \to (\pi,0) \to (\pi,\pi) \to (0,0)$ in the 2D BZ. We have divided out all $|X(\mathbf{q},\omega)|^2$ by k_BT.

In the bottom panel, we've plotted the lineshapes at three characteristic momenta $((0,0),(\pi/2,\pi/2),(\pi,\pi)$ in terms of their T dependence. Here small changes are observed on increasing temperature as one goes from the harmonic to the anharmonic regime. The (π,π) mode is most sensitive to this effect, whereas the lineshapes at BZ center don't respond appreciably.

The asymptotically low temperature regime is understandable in terms of an effective harmonic model. The assumption is that the deviation of displacement fields from the checkerboard ordered ground state pattern is small. The most general distortion cost one can write to quadratic order is: $V^{(2)}_{\text{eff}} \approx \sum_{i,j} b_{ij}\Delta x_i \Delta x_j$, where the $\Delta x_i = x_i - x_i^0$, with x_i^0 being the distortion in the $T = 0$ CO state. The resulting Langevin equation is linear in Δx_i, but spatially coupled, and can be solved by Fourier transformation. The b_{ij} can be obtained from an expansion of the ground state energy; $b_{\mathbf{q}}$ is its Fourier transform. The power spectrum that emerges has the form:

$$|X(\mathbf{q},\omega)|^2 = \frac{2\gamma k_BT}{|f(\mathbf{q},\omega)|^2}$$
$$f(\mathbf{q},\omega) = (-M\omega^2 + b_{\mathbf{q}} + i\gamma\omega). \quad (7)$$

The dispersion, found by plotting the peak locations at low temperature, $T = 0.1T_c$, has been fitted in Fig. 5 to obtain the coefficients of nearest and next-nearest neighbor contributions in $b_{\mathbf{q}}$. The fit parameters are $K_{\text{eff}} = 0.78$ and $J = 0.09$, respectively, the local stiffness and the nearest neighbor coupling. The further neighbor contributions are significantly smaller, owing to the gap in density of states of the ordered state. The dispersion compares well with a 'random phase approximation' (RPA) calculation done on the $T = 0$ CO background, using the static polarizability, $\Pi(\mathbf{q},\omega = 0)$.

The departure from harmonic behavior with increasing T can be motivated by using a cubic term in the energy,

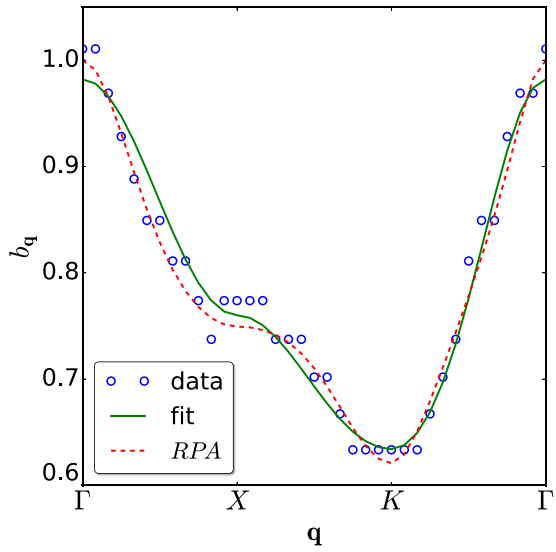

FIG. 5. Fitting the dispersion $b(\mathbf{q})$ using harmonic functions on the BZ at the lowest $T = 0.1T_c$. We find that a nearest neighbor model is reasonably accurate in describing the dispersion of mode values. The blue open circles are extracted from the data, green solid line is the best fit with free parameters K_{eff} and J, and the red dashed curve features RPA result computed using the perfect ordered state at zero T. The obtained fitting parameters are $K_{\text{eff}} = 0.78$ and $J = 0.09$, which denote the effective local stiffness and the nearest neighbor intersite coupling, respectively.

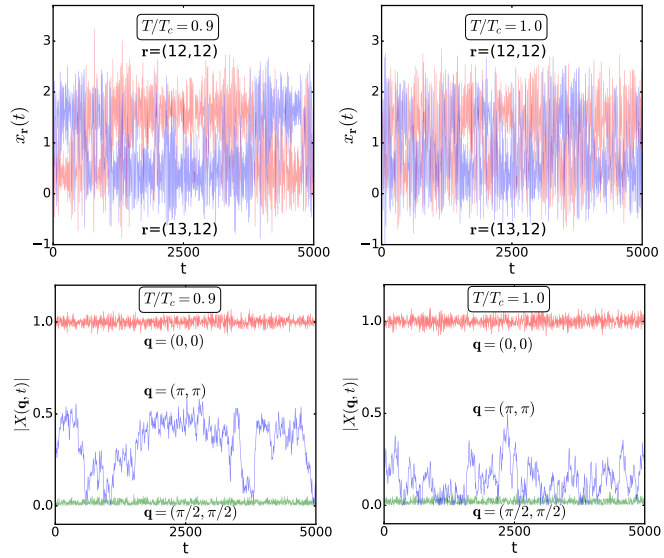

FIG. 7. Top panel: Trajectories of nearest neighbor sites for part of the full time series. We see 'resident flips' first appearing in the left figure ($0.9T_c$). The nearest neighbors switch in mean values and stay for tens of oscillation timescales. Moving to the actual T_c, featured in the right figure, we see more frequent exchange moves that ultimately leads to vanishing of $S(\pi, \pi)$. Bottom panel: Corresponding Fourier mode trajectories at the same temperatures. The mean values are retained and actual trajectories are shown without shifting, as opposed to the low T figure. We see the special behavior of the (π, π) mode quite clearly near criticality. Large oscillations feature in the left figure while a reduction of mean value to near zero is visible at T_c.

below. The energy cost with cubic terms has a form: $V^{(3)}_{\text{eff}} = \sum_{ij} b_{ij}\Delta x_i \Delta x_j + \sum_{ijk} c_{ijk}\Delta x_i \Delta x_j \Delta x_k$ Fourier transforming the Langevin equation leads to

$$f(\mathbf{q}, \omega)X(\mathbf{q}, \omega) = \xi(\mathbf{q}, \omega) - \alpha(\mathbf{q}, \omega),$$

where $\alpha(\mathbf{q}, \omega) = \sum_{\mathbf{q}',\omega'} C_{\mathbf{q},\mathbf{q}'} X(\mathbf{q} - \mathbf{q}', \omega - \omega')X(\mathbf{q}', \omega')$. This can be dealt with perturbatively by substituting the harmonic solution in the nonlinear term. One formulates the perturbation expansion in terms of the response function $\langle X(\mathbf{q}, \omega)\xi(-\mathbf{q}, -\omega)\rangle$. The Fourier transformed variable $X(\mathbf{q}, \omega)$ has an expansion in powers of the anharmonic coefficient. This has the first nonvanishing correction for the response function at second order, as odd order correlators of the noise vanish by symmetry. The effective "self-energy" $\Sigma(\mathbf{q}, \omega)$ that emerges has the form:

$$\Sigma(\mathbf{q}, \omega) = \left\langle \sum_{\mathbf{q}',\omega'} \frac{\xi(\mathbf{q} - \mathbf{q}', \omega - \omega')\xi(\mathbf{q}', \omega')}{f(\mathbf{q} - \mathbf{q}', \omega - \omega')f(\mathbf{q}', \omega')} \right\rangle,$$

where angular brackets denote averaging over the noise variable. This is an $O(T)$ quantity at this level. The real and imaginary parts of this corrects the pole location and damping,

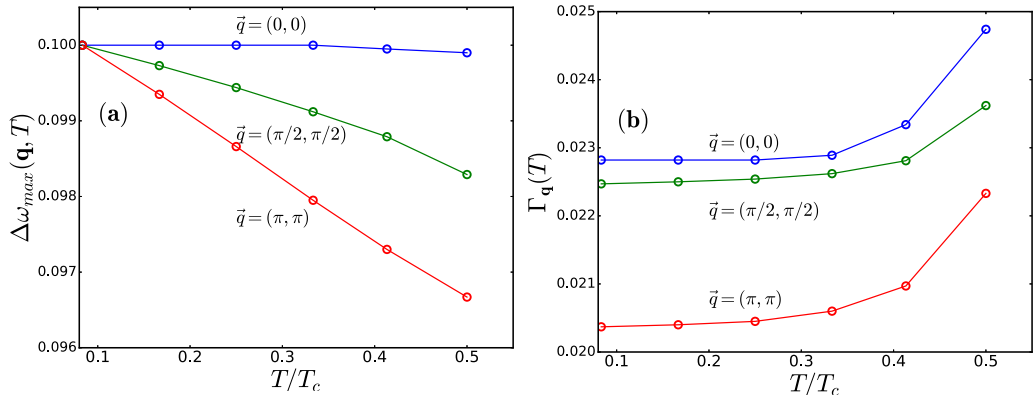

FIG. 6. Quantifying the effect of anharmonicity. Left: $\Delta\omega_{\max}(\mathbf{q}, T)$: the difference of peak locations from that at $T = 0$, and right: the linewidth $\Gamma_{\mathbf{q}}(T)$. Results are for three characteristic momenta: (0,0), $(\pi/2, \pi/2)$, and (π, π). We see linear softening of mode values and an initially linear increase in damping for all momenta. Nonlinear corrections take over in the latter as one raises the temperature.

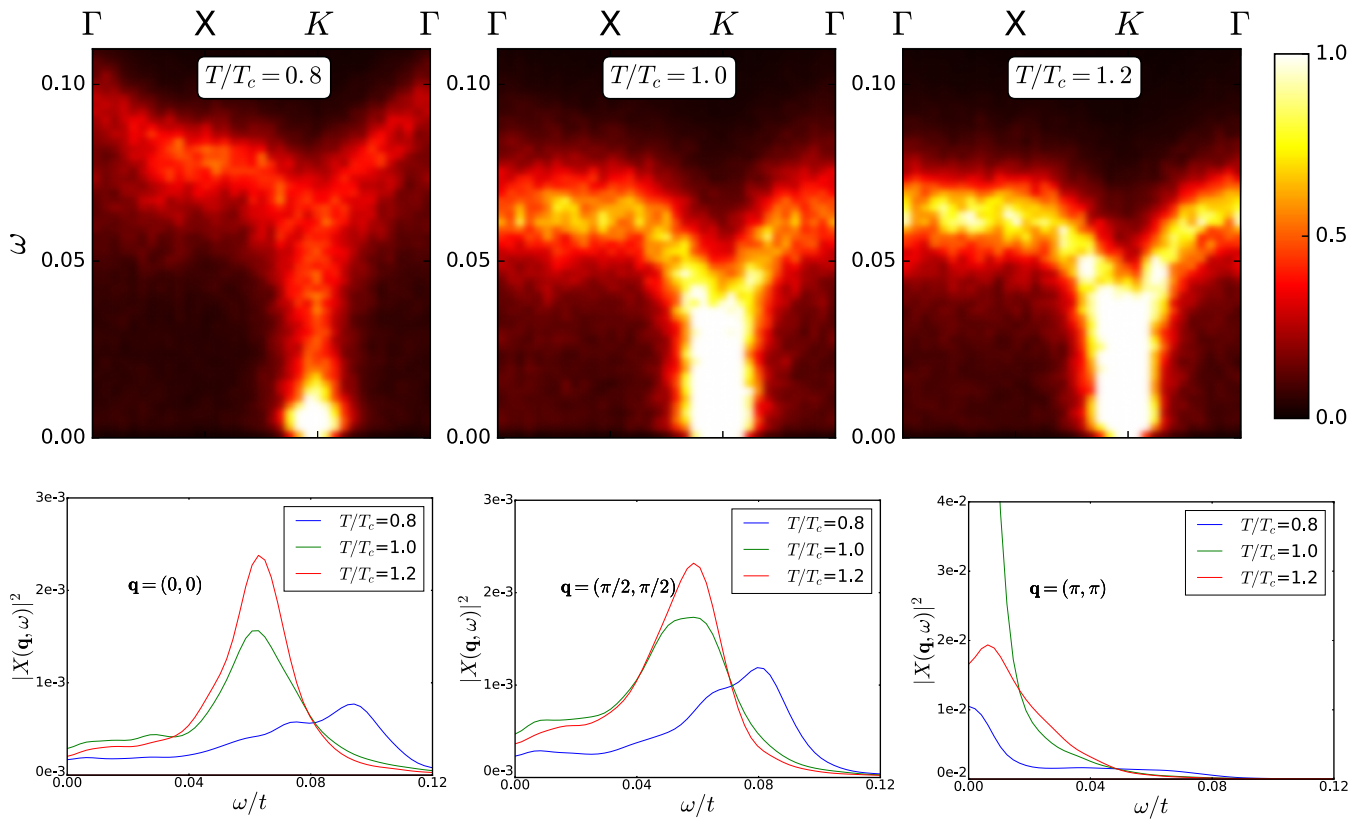

FIG. 8. Top row: Maps of the power spectrum $|X(\mathbf{q},\omega)|^2$ in the vicinity of T_c. The spectral intensities are plotted with the momentum trajectory $(0,0) \to (\pi,0) \to (\pi,\pi) \to (0,0)$ along the x axis. Bottom row: Lineshapes at corresponding temperature points for three momentum points along the BZ diagonal: (0,0), $(\pi/2, \pi/2)$, and (π,π). All power spectra are normalized by $k_B T$.

respectively, with the corrections varying linearly with T for a fixed $\mathbf{q}$.

Fig. 6 indicates that the frequency shift and increase in broadening indeed have a leading linear T behavior at low temperature. The damping features nonlinear corrections in T as one heats up, which arise from 'stray flips' (SF) which are large, isolated exchange of displacements on the lattice. The slope of the linear part is of course $\mathbf{q}$ dependent and the nature of this dependence is monotonic along the BZ diagonal.

B. Critical fluctuations: $T \sim T_c$

1. Real time trajectories

The trajectories in both real and momentum space for this regime are shown in Fig. 7. The top row depicts nearest neighbor displacement time series. New events show up compared to low T, in the form of 'exchange moves' between large and small distortions. The left figure ($T/T_c = 0.9$) shows a clean version of what may be called a 'resident flip' (RF), where the exchanged distortions don't flip back within a short

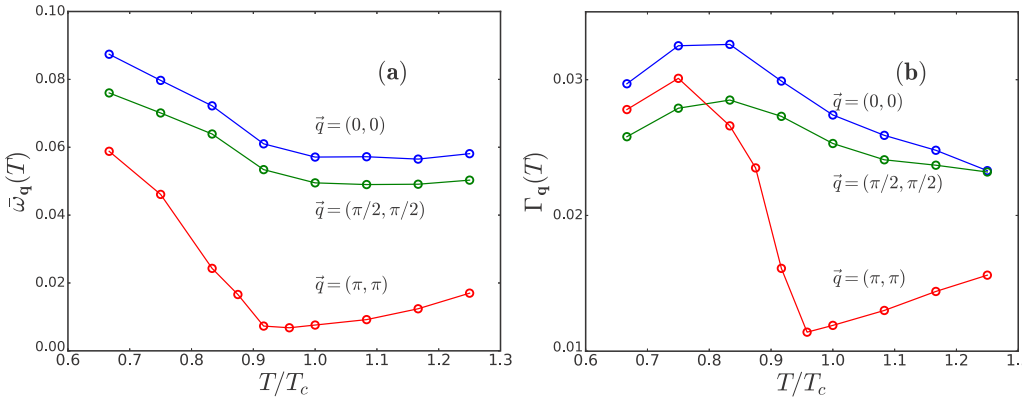

FIG. 9. Fits to extract the mean frequencies ($\bar{\omega}$) and standard deviations ($\Delta\omega$) as functions of temperature. The left panel features mean curves, showing an overall softening trend that's most prominent at (π,π). The right panel features damping rates, where a nonmonotonicity is seen in the thermal behavior. At T_c, the (π,π) mode is again sharp.

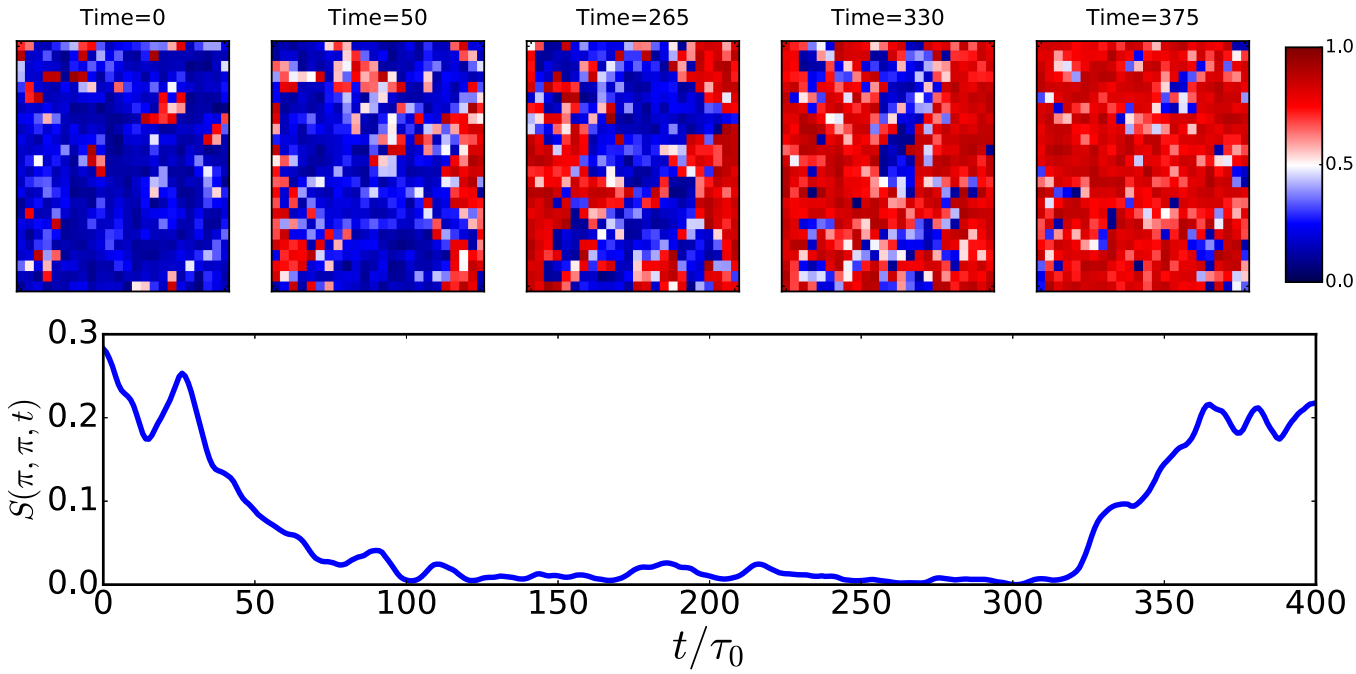

FIG. 10. Top panel: Growth of a large domain is shown through taking the actual configurations and subtracting out the prevalent checkerboard pattern C. Bluish regions indicate perfect order alla C and red regions denote the opposite pattern of checkerboard ordering C'. The white areas are indicative of boundaries between these two patterns. Time is measured in units of τ_0, the bare oscillation timescale. Bottom panel: The instantaneous structure factor $S(\pi,\pi,t)$ shown across the time interval of domain growth. Dominant order alla C or C' result in increased value, while in the middle panel we observe a near zero value due to almost equal size of the two domains.

($\sim$5–10τ_0) timescale. Moving closer to the actual T_c, their frequency increases. These events have associated spatial correlations as well, which trigger domain growth and shrinkage, as discussed later. Ultimately, these lead to destruction of order as a whole.

The bottom row of Fig. 7 shows trajectories of different momentum modes. This time the mean values are shown without shifts. As before, we observe the benign nature of (0,0) and $(\pi/2,\pi/2)$ modes. The (π,π) mode, however, features large oscillations just before T_c, whose mean value drops rapidly on approaching criticality. The dynamical event responsible for this is domain growths, taking place over the full lattice. We will discuss this later.

2. *Power spectrum*

Moving to the frequency dependent indicators, far richer behavior is seen here compared to low temperatures. The top row of Fig. 8 depicts spectral maps of $|X(\mathbf{q},\omega)|^2$. In the leftmost figure ($T = 0.8T_c$), a faint low energy feature is seen emerging near (π,π). A more complete weight transfer is observed in the middle panel ($T = T_c$). This originates from 'exchange moves' discussed before in the context of trajectories. They have an associated timescale that is much larger ($\sim$100 times) than the bare oscillation period.

Low energy spectral weight arises from these moves. Stray flips (SF) start occurring around $0.6T_c$, whereas RF's discussed before only show up around $0.9T_c$. The spectrum just past criticality (right panel) has a different dispersive character compared to lower T and is considerably more broad around (π,π). The lineshapes at three characteristic momenta (0,0), $(\pi/2,\pi/2)$, and (π,π) feature in the bottom row of Fig. 8. A gradual spectral weight transfer to lower frequencies is observed in the first two on heating close to T_c, whereas a dramatic near-zero frequency weight develops at (π,π). The intensity also, even after being divided out by a factor of k_BT, is $\sim$10 times here at T_c.

In Fig. 9, we've shown mean frequencies (left panel) and standard deviations (right panel) across the BZ diagonal in this regime. The softening at the BZ boundary is quite prominent on approaching T_c. The overall branch also changes its character compared to low T. In the dampings, a nonmonotonic

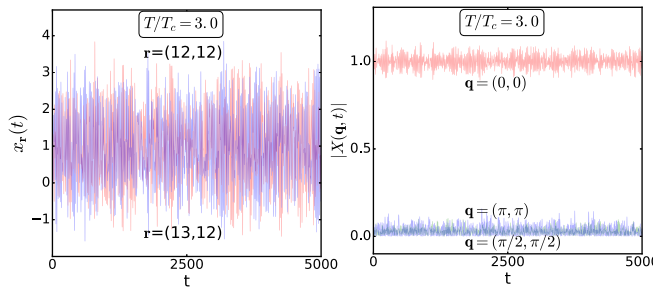

FIG. 11. Left: Trajectories of nearest neighbor sites for part of the full time series. We see flip moves merging with large amplitude oscillations. This leads to broad but unimodal power spectra in this regime. Right: Corresponding Fourier mode trajectories at the same temperatures. The mean values are retained and actual trajectories are shown without shifting, as opposed to the low T figure. Both the $(\pi/2,\pi/2)$ and (π,π) trajectories oscillate above zero, indicating loss of spatial correlations in the dynamics.

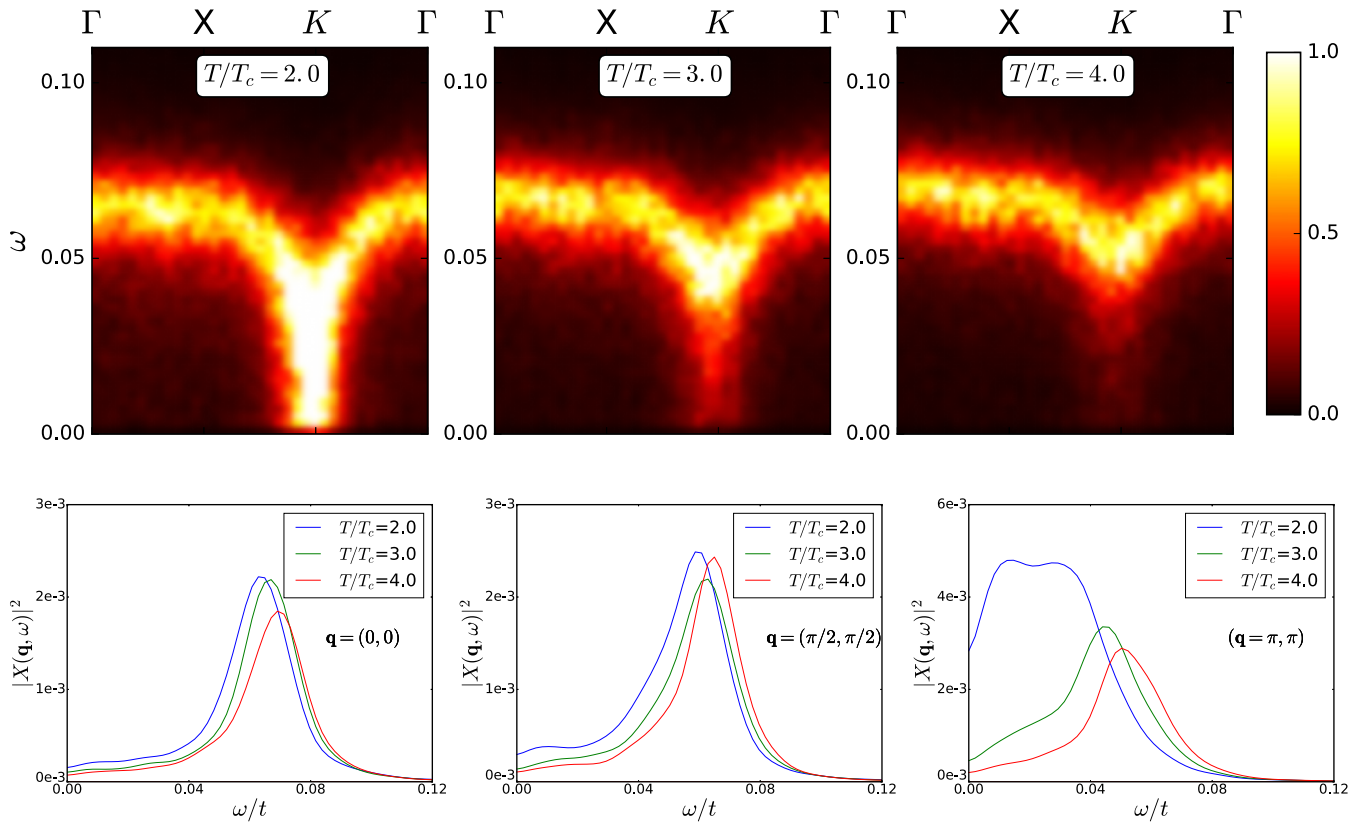

FIG. 12. Top row: False color maps of the power spectrum $|X(\mathbf{q},\omega)|^2$ in the disordered polaron liquid regime. The spectral intensities are plotted with the momentum trajectory $(0,0) \to (\pi,0) \to (\pi,\pi) \to (0,0)$ along the x axis. Bottom row: Lineshapes at corresponding temperature points for three momentum points along the BZ diagonal: (0,0), $(\pi/2, \pi/2)$, and (π,π). All power spectra are normalized by $k_B T$.

trend is seen, also most prominent at (π,π). The width of the spectrum at this momentum is actually resolution limited, rather than γ limited. Hence, this is a universal feature, irrespective of microscopic details.

3. *Domain dynamics near T_c*

The ground state of the present problem is (π,π) ordered, which corresponds to a checkerboard pattern. There exists two energetically degenerate patterns, related to each other by a Z_2 transformation. We call them C and C'. Up to temperatures of $\sim 0.6T_c$ while there are occasional 'flips' caused by thermal kicks, the site quickly reverts to its original state—we call these events stray flips (SF). There is no domain growth. However for $T \gtrsim 0.8T_c$ large amplitude fluctuations can combine with the tunneling events to create a cascade event.

In Fig. 10, we depict a domain growth event as a function of time from our data at $T/T_c = 0.9$. The bluish regions depict 'C' kind of order, which dominates initially. However, with increasing time, the opposite pattern C' tries to grow from within and the structure factor $S(\pi,\pi,t)$ decreases as a consequence. In the middle, we see a low structure factor where two kinds of domains are almost equally present. Later, the C' order encompasses the lattice and $S(\pi,\pi,t)$ grows again. These 'domain oscillations' typically take place over a large ($\sim 500\tau_0$) timescale.

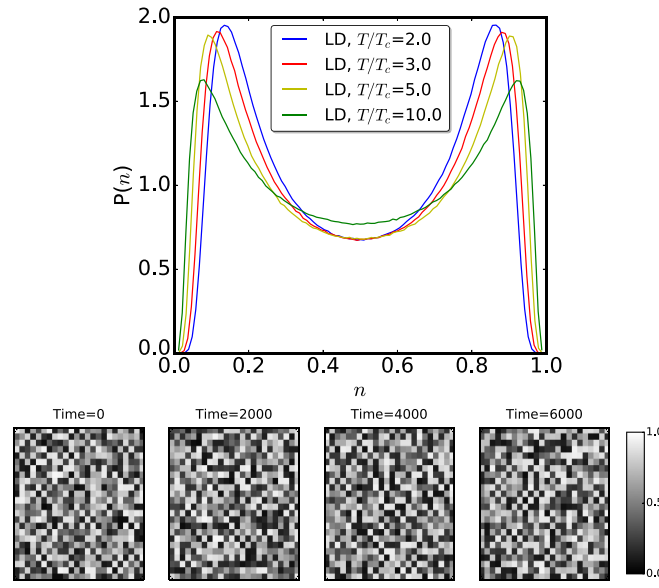

FIG. 13. Top panel: The distribution of local density $P(n)$ showing distinct bimodal features until $\sim 10T_c$. This means there's a large region in temperature where polarons are present in the lattice, but there's no global ordering. Bottom panel: Snapshots from time evolution at $T = 3.0T_c$. One sees dynamic patterns of short-range correlated polarons, hinting a nontrivial spatial structure.

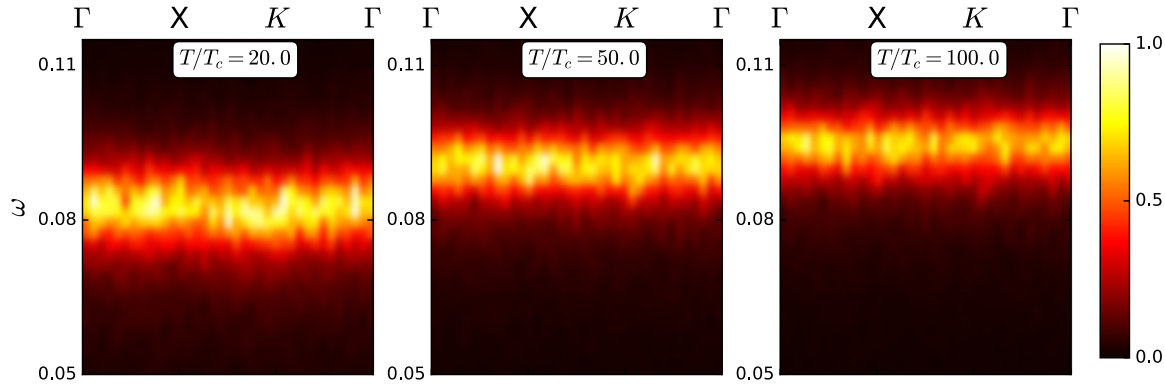

FIG. 14. False color maps of the power spectrum $|X(\mathbf{q}, \omega)|^2$ in the high T regime. The spectral intensities are plotted with the momentum trajectory $(0, 0) \rightarrow (\pi, 0) \rightarrow (\pi, \pi) \rightarrow (0, 0)$ along the x axis.

C. Polaron liquid: $T_c \ll T < T_P$

In this regime long-range order is lost but there are short-range correlations still prevalent amongst large distortions. There is no obvious small parameter or a universal phenomenology as in the critical regime.

1. Real time trajectories

The left panel of Fig. 11 features real space trajectories on nearest neighbors at $T = 3.0T_c$, where one sees a merger of large oscillations and flip moves. The corresponding momentum trajectories at this temperature are all featureless, as observed in the right panel.

2. Power spectrum

The power spectra (top panel in Fig. 12) display a mildly dispersive band with pronounced softening and broadening near (π, π). The dip gradually reduces on heating up, signifying loss of intersite correlations. There's also a mild stiffening of the branch as a whole with increasing T. On heating up even further, one sees the branch lose dispersion at $\sim 10T_c$. The broadening also becomes γ limited eventually. This signifies that the effective Hamiltonian for the oscillators first reduces to a local one and then the anharmonicities vanish at asymptotically high T.

The lineshapes at specific momenta corroborate the conclusions drawn above. At lower T, the damping is highest at the BZ corner. The mode values shift on heating up. There's a quantitative reduction in damping on heating for all momenta, the most noticeable being (π, π).

The corresponding density distributions and snapshots are highlighted in Fig. 13. In the top panel, we do see prominent bimodality for an extended range of temperatures ($2T_c$–$10T_c$). This is indicative of the fact that polarons and their short-range correlations (shown in the bottom panel) dictate the physics in this regime.

D. Polaron dissociated phase: $T \gtrsim T_P$

In the high T regime, the power spectrum gradually loses dispersive features and is broadened compared to its low T counterpart. Intuitively, these features can be explained using an effective Hamiltonian with a nonlinear local term and a nearest neighbor harmonic part for the x_i field. The local term may be derived by tracing out electrons from a single site Holstein problem. The nearest neighbor coefficient is of order $J \sim \frac{t^2}{E_p}$. The dimensionless form of the full Langevin equation reads

$$\frac{d^2X_i}{d\tau^2} = -\gamma' \frac{dX_i}{d\tau} - X_i + \langle n_i \rangle + \sqrt{\frac{k_B T}{E_p}}\eta_i, \tag{8}$$

where $\gamma' = \gamma/M\omega_0$, $\tau = \tau_0 t$, and $X_i = (g/K)x_i$. The noise correlator is given by

$$\langle \eta_i(\tau)\eta_j(\tau')\rangle = \gamma' \delta_{ij}\delta(\tau - \tau'). \tag{9}$$

At asymptotically high temperature, $T \gg E_p$, the density becomes a local, linear function of X_i and the corresponding power spectrum becomes identical to that of a single harmonic oscillator with a renormalized frequency. This frequency approaches the bare value at asymptotically high temperature. On lowering T, higher order corrections in βE_p feature in the $\langle n_i \rangle$. We have a linear, $\mathcal{O}(\beta E_p)$, correction to the bare stiffness featuring first, and then a $\mathcal{O}(\beta^3 t^2 E_p)$ intersite correction which gives rise to 'dispersion.' In Fig. 14, the power

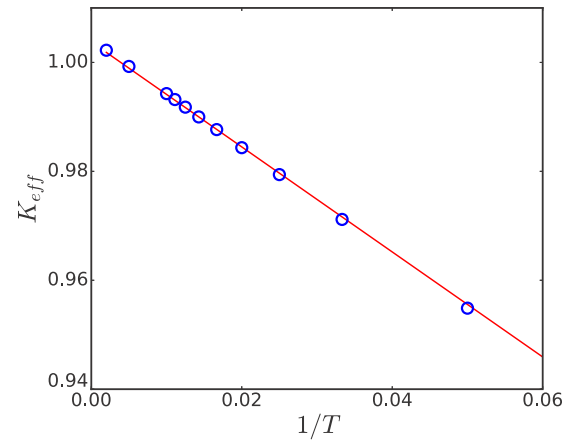

FIG. 15. Effective stiffness (K_{eff}) plotted against $1/T$ in the asymptotically high T regime. A linear fit (consistent with a high T expansion) is in fairly good agreement with the data. Ultimately, for small $1/T$, one gets back to the bare stiffness value $K = 1$.

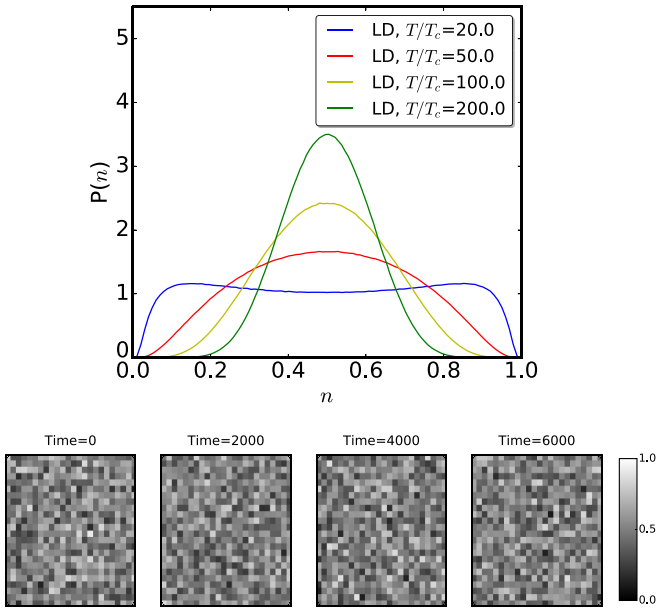

FIG. 16. $P(n)$ and spatial character in the 'polaron dissociated' phase. The top panel depicts a broad distribution at the lowest temperature shown ($T/T_c = 20.0$) gradually sharpening to a nearly gaussian distribution with mean $n = 0.5$ at very high temperature ($T/T_c = 200.0$). The spatial character shows 'melted' polarons, which don't have any interesting dynamics.

spectra in this regime are featured, which ceases to show dispersive features and only exhibits gradual band tightening, with reduction in damping as one heats up.

In Fig. 15, we fit the effective stiffness, calculated from the $P(x)$ distributions against $1/T$. One expects a linear variation from an analytic high T expansion, which is borne out by the actual data.

The density distribution and snapshots from dynamics in this regime are shown in the top and bottom panels of Fig. 16, respectively. The distributions converge to a gaussian at large enough T, with a mean $n = 0.5$ and width proportional to $\sqrt{T}$. The snapshots exhibit 'melted' polarons, which are represented as grayish regions.

V. DISCUSSION

In what follows, we comment on (i) some aspects of indicators, parameter choice, and methods, then (ii) computational checks that we have carried out on γ dependence, system size, etc., then (iii) discuss 'toy models' that can provide some analytic insight, (iv) comment on how our results can be related to real life phonon data, and finally (v) comment on other problems that the Langevin approach can access.

A. Comment on indicators, method, etc.

1. D_{nn} vs D_{xx}

The evolving dynamical variable of our equations is the displacement field $x_i(t)$. Hence, the analysis of spectra was done by Fourier transforming this field directly. However, in INS experiments, the physical quantity accessed is the dynamical structure factor, which is basically the Fourier transform of the pair correlation function $\langle n_i(t) n_j(t') \rangle$. In the present scheme, the same quantity may also be calculated within the adiabatic approximation.

We compared the power spectra of the x_i and n_i fields to check the correspondence, Fig. 17. Over the full range of temperatures, the lineshapes at characteristic momenta agree in terms of moments calculated on the normalized distributions. The overall intensities are different, as the n_i field is constrained to take values between 0 and 1. Apart from that, the $D_{nn}(\pi, \pi, \omega)$ lineshapes reveal that the critical behavior is more acutely sensed by the density field than the x_i. The signatures of anharmonicity and 'stray flips' (SF) also seem to show up at somewhat lower T in the D_{nn} spectra compared to the D_{xx} ones.

2. Effect of coupling change

The present study is focused on a specific intermediate coupling value $g = 2.0$. This is a particularly stable choice with respect to the type of numerics used and allows for equilibration within a reasonable time. The main observations on increasing coupling are: (i) the structure factor $S(\pi, \pi)$ becomes flatter near $T = 0$, owing to weaker harmonic oscillations, (ii) the low temperature dispersion, especially the dip near (π, π) becomes subdued, (iii) the critical behavior is 'cleaner,' in the sense that stray flips (SF) become rarer and the resident flips (RF) are sharper as amplitude fluctuations are suppressed. The dynamics near criticality shows the emergence of three bands: the 'harmonic' band, one near $\omega = 0$, and an intermediate one. The low-frequency weight transfer becomes less **q** selective compared to $g = 2.0$. However, since equilibration itself is problematic for higher g (requires large run times) and the flip times are also quite large compared to those at $g = 2.0$, the trustability of the dynamical features for a limited run length becomes doubtful.

The understanding of critical dynamics is more transparent at stronger coupling (e.g., $g = 4.0$), where the problem truly maps on to an Ising system. In that limit the adjacent sites have a large difference in mean displacements and the effective potential for two sites embedded within a checkerboard background is a double well with two deep minima. As $T \to T_c$ only cooperative 'resident flips' (RF) would dictate critical behaviour there. This eliminates the anharmonic amplitude fluctuation effects that complicate the analysis in our more realistic $g = 2$ case.

3. Langevin vs the 'PSPA' approach

We quickly comment on another approach through which large amplitude phonon displacements can be accessed. The adiabatic version of the method is called the 'static path approximation' (SPA) and retains only the $\omega_n = 0$ Matsubara mode of the displacement field. There are no 'phonons' in this scheme. Phonons emerge when an additional Gaussian expansion is made on top of the SPA theory—leading to the perturbed SPA (or PSPA) approximation [34]. The Langevin scheme and PSPA, we feel, are competing approaches to strong coupling phonon physics and a comparison may be useful.

Langevin dynamics allows one to access large amplitude dynamical fluctuations in real time at the classical level. These

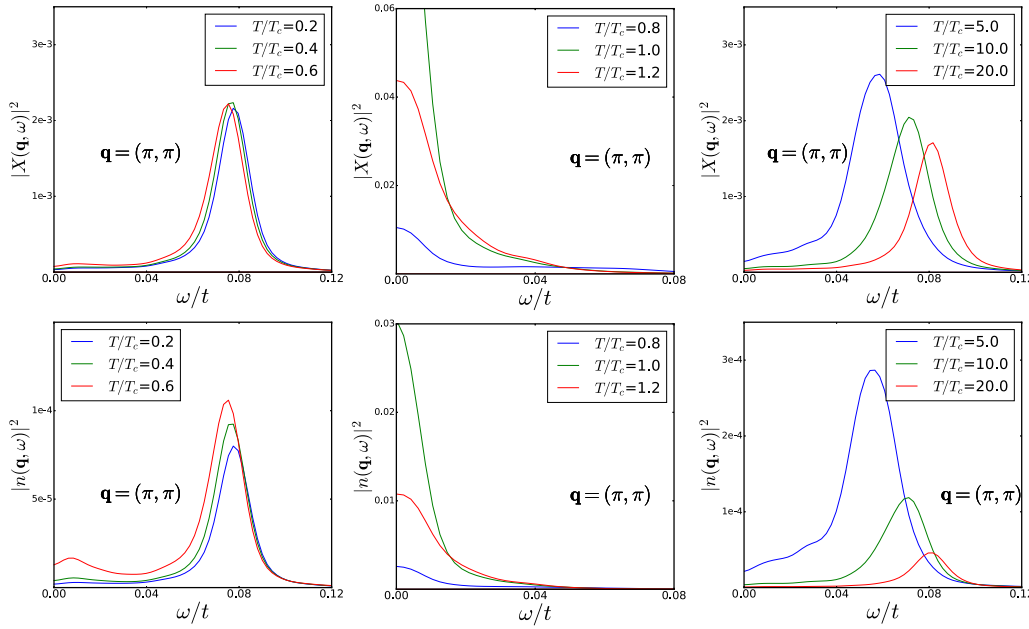

FIG. 17. Comparison of $D_{xx}(\omega)$ (top panel) and $D_{nn}(\omega)$ (bottom panel) spectra for three characteristic temperature regimes: (i) low temperatures (left)—the stray flips are detected more acutely by the density spectra, causing low energy weight transfer, (ii) near T_c (middle)—the spectra are very similar, even the intensities are of the same order, (iii) high T (right)—the shift of mode frequencies is present similarly in both spectra, but intensities fall sharply in the latter.

fluctuations naturally die off as $T \to 0$. PSPA is more accurate at low T. Although it misses subtle instanton effects it treats phonons quantum mechanically, uses the full frequency-momentum dependence of the electronic polarizability to compute the spectra, and yields phonon broadening without need for any ad hoc damping parameter. If one were to be interested in low T physics in the strong coupling system PSPA is the better choice.

Over a wider T window, however, the Langevin approach has an advantage. The thermal transition is driven by 'flip moves' wherein the displacement value at a given site changes by a large amount. *This is not a Gaussian fluctuation.* So, when thermal tunneling of the displacement variable becomes relevant, from a fraction to T_c all the way up to T_p, the Langevin approach has a clear advantage. Ideally an equation of motion approach with a more complex, and self-consistent, noise and damping would be a method accurate all the way from low to high T.

B. Computational checks

1. Dependence of results on γ choice

The ordering peak in the structure factor for different γ values has an overall similarity. The lower $\gamma = 0.1$ gives a slightly higher T_c. The $\gamma = 0.5$ and $\gamma = 1.0$ curves lie on top of each other, signifying the insensitivity of the system's equal-time properties on this parameter [shown in Fig. 18(a)]. However, we comment that if one uses a much higher γ, the problem ceases to have a correspondence with the physical Holstein model and becomes overdamped.

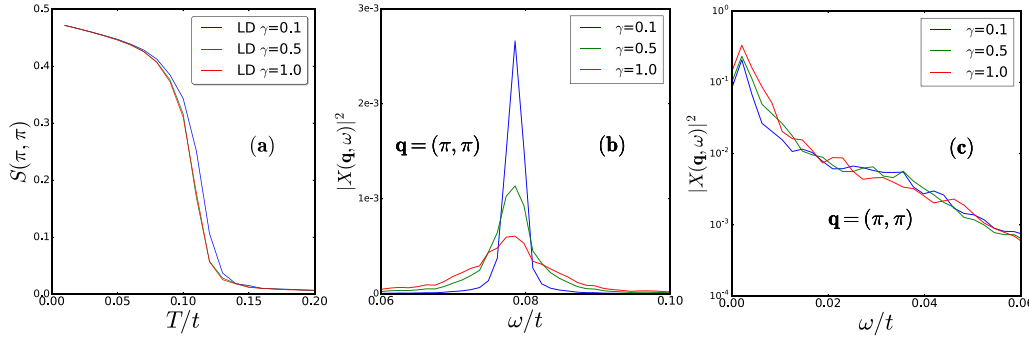

FIG. 18. (a) The structure factor (π, π) at $T = 0.2T_c$ for three different γ values (0.1,0.5,1.0). The $\gamma = 0.1$ result features a slightly higher T_c compared to the other two. There's a 'saturation' at higher γ, whose results coincide with one another. (b) The (π, π) lineshape in the low T harmonic regime. The broadening is observed to increase proportionately with γ, as expected from the harmonic oscillator result. (c) The (π, π) lineshapes at T_c plotted on a logarithmic scale. The γ variation is significantly suppressed in this critical regime.

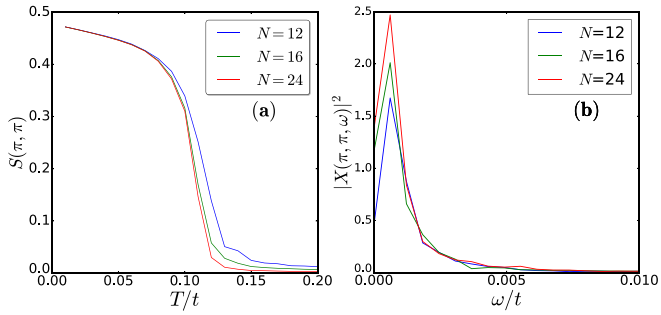

FIG. 19. (a) The structure factor $S(\pi,\pi)$ characterizing order-disorder transition for three different sizes (12×12, 16×16, 24×24). The γ value is 1.0 for all of them. We see a mildly sharper transition for the largest size. (b) Power spectra at (π,π) for different sizes. The character is similar for all the profiles, with a growing weight near zero frequency for larger sizes.

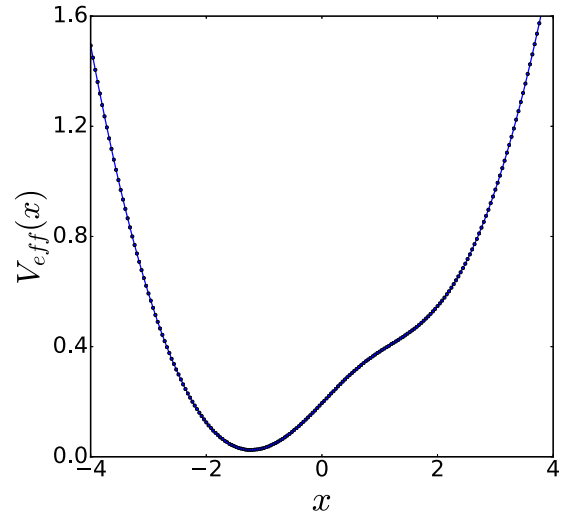

FIG. 20. Effective potential for the 'embedded two-site' problem plotted against the difference in displacements $x=(x_1-x_2)$ of the two sites. The background order is a perfect checkerboard with distortions 0 and g/K, respectively. The potential is obtained by keeping x_1+x_2 fixed, which ensures number conservation locally. The look is that of an asymmetric double well with an extremely shallow second minimum. The oscillation frequency at the harmonic level about the lower well is 0.054 and that about the overall profile (relevant at very high temperature) is 0.069. The potential is indeed harmonic at large range. The splitting between the two minima is $\Delta=0.38$.

To establish the dependence of power spectra on γ, we look at two different temperature regimes: (i) the low T harmonic regime and (ii) the critical regime ($T\sim T_c$). The observations are featured in Figs. 18(b) and 18(c), respectively. In the former, increasing γ by a decade (0.1–1.0) has a proportionate impact on the broadening of the (π,π) lineshape. This is expected from the analytic form of the power spectrum. On the other hand, near T_c the dependence on γ is weak. We have superposed the (π,π) lineshapes on a logarithmic scale for three different γ values to show this. The conclusion is that the critical behavior is universal and doesn't depend crucially on microscopically generated dissipation scales.

2. Size dependence

We have checked size dependence of the $S(\pi,\pi)$, which characterizes the order-disorder transition and the (π,π) lineshapes at criticality. The results are displayed in Figs. 19(a) and 19(b), respectively. The former shows a sharper transition as we go to bigger sizes (16×16 to 24×24), as expected. The low to intermediate temperature behavior, governed by linear phonon excitations, is very similar for all sizes. The latter quantity has a width that is basically resolution limited for all sizes. The weight at 'near-zero' frequency increases nominally with size. We expect an infinitely sharp peak at zero frequency in the thermodynamic limit.

C. Simple models for the different regimes

1. Noncritical behavior

We attempted an explanation of the features found in the power spectrum for wave vectors near the zone boundary through a single variable toy model. It misses the collective critical dynamics but gives a fairly good account of 'beyond harmonic' physics at low to intermediate temperatures and also the high T regime.

The model problem constructed is a two-site Holstein dynamics embedded in the background of the $T=0$ mean-field state, which is (π,π) ordered. The sum of coordinates (x_1+x_2) is held fixed, to ensure particle density conservation, while (x_1-x_2) is varied to first generate an effective potential numerically. Then, the dynamics of the 'collective coordinate' is studied within this potential. Although, in the real problem, there's no density conservation locally, the present simplification is a good enough approximation at least for $T<T_c$.

The look of this effective potential (shown in Fig. 20) is that of an asymmetric double well at low values of (x_1-x_2), with a very shallow second well. The difference in well depths is due to correlation energies arising from the background order. Hence, the energy splitting Δ between the two minima is comparable to T_c in the actual problem. At asymptotically large values of (x_1-x_2), the potential is harmonic, whose stiffness can be extracted numerically. Hence, the profile can't be fitted to any polynomial function over the full range.

The dynamics features three timescales: (i) the oscillation time about the deeper well ($\tau_{\mathrm{osc},1}$), where the initial condition is chosen to lie, (ii) τ_{flip}, for excursions to the shallower well, and (iii) the oscillation time about the overall potential profile ($\tau_{\mathrm{osc},2}$). These become accessed gradually as one increases T. The frequency scales corresponding to (i) and (iii) are 0.054 and 0.069, respectively.

We've analyzed the power spectrum of the difference coordinate $|(x_1-x_2)(\omega)|^2$ for various values of the scaled temperature T/Δ, where Δ is the energy splitting between two wells. The frequencies are scaled with respect to Ω (the bare oscillation frequency) in the real problem and $\omega_{\mathrm{osc},2}$ in the model situation. Figure 21 [panels (a) and (b)] shows the result. Figure 21(a) is for the model problem, whereas 21(b) is for the actual dynamics.

The gross behavior is simple—at low enough T/Δ, harmonic dynamics about the deeper well is observed, with the characteristic frequency related to its stiffness. At slightly

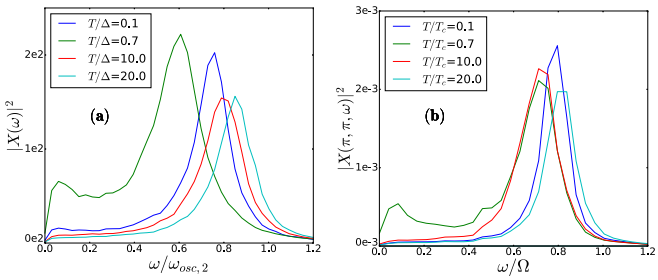

FIG. 21. (a) Spectra of the model problem ($|(x_1 - x_2)(\omega)|^2$) compared with (b) the actual power spectrum of the full problem at (π, π). A visual similarity is apparent for both the low and high T regimes. Frequencies are scaled with respect to $\omega_{\mathrm{osc},2}$ in the former and Ω in the latter case. Temperatures are featured in units of Δ for the model problem and T_c for the full problem.

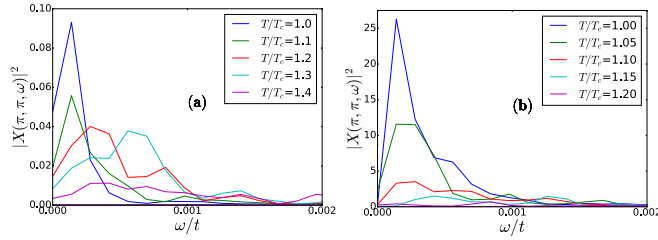

FIG. 22. (a) Spectra of the Ising problem compared to the actual power spectra (b) of the full problem at (π, π). A visual similarity is apparent close to T_c, where other details are irrelevant. Frequencies are scaled with respect to J in the former and t in the latter case. Temperatures are featured in units of T_c for the respective problems.

higher temperatures, anharmonic effects result in well shift and quantitatively larger damping. Then, the flips to the shallower well start showing up, with $\tau_{\mathrm{flip}} \gg \tau_{\mathrm{osc},1}$. This results in an accumulation of spectral weight near zero frequency. For $T/\Delta \gg 1$, the oscillations take place about the overall profile. The peak shifts towards a frequency consistent with the corresponding stiffness and damping again becomes γ limited.

2. Critical behavior

We attempted to understand the critical behavior in terms of dynamics of an Ising model with nearest neighbor AF coupling. Since this is a discrete variable model, the dynamics was designed in terms of the 'sign' of the evolving degree of freedom, following a recent study [35]. The equation of motion (in discrete form) is

$$H = J \sum_{\langle ij \rangle} S_i S_j$$

$$S_{i,t_{n+1}} = sgn\left(S_{i,t_n} - \epsilon * \frac{\partial H}{\partial S_i} + \sqrt{\epsilon} * \eta_{i,t_n} \right). \qquad (10)$$

The parameters for this problem were: $J = 1$ and $\epsilon = 0.01$. The noise has the properties

$$\langle \xi_i(t_n) \rangle = 0$$

$$\langle \xi_i(t_n) \xi_j(t_m) \rangle = 2k_B T \delta_{ij} \delta_{nm}.$$

This can be interpreted as an overdamped Langevin equation, from which the critical dynamics can be extracted along with the thermodynamics. The power spectrum of this model at (π, π) has a Lorentzian profile about zero, whose width collapses as one tunes the temperature near T_c ($\sim 2.2J$) from above. At higher T, one observes gradual broadening, related to the reduction of correlation length. A direct comparison of the lineshapes between this model and the real problem at (π, π) is shown in Figs. 22(a) and 22(b). The temperatures are normalized by the respective T_c scales.

The coarse-grained, continuum limit of the AF Ising system with a conserved magnetization density, relevant to the present Holstein model, falls under Model B amongst the dynamical universality classes, introduced by Halperin and Hohenberg [32]. This model in the Gaussian limit ($T \gg T_c$) can be solved analytically to yield a Lorentzian power spectrum, whose width collapses on approaching T_c from above.

Let $S(q, \omega)$ be the coarse grained spin field. The power spectrum is obtained by multiplying two factors of this field and averaging over the noise, which gives

$$\langle S(q, \omega) S(q', \omega') \rangle = C(q, \omega)(2\pi)^{d+1} \delta(q + q') \delta(\omega + \omega')$$

$$C(q, \omega) = \frac{2k_B T D q^2}{\omega^2 + (Dq^2(r + q^2))^2}.$$

This profile is a Lorentzian and has width that is almost $Dq^2 r$ for $T \gg T_c$ and almost Dq^4 for $T \sim T_c$. Hence, we have a diminishing width (strictly zero for $q \to 0$) as one approaches T_c from above.

D. Experimental signature

Several recent experiments suggest an anomalous behavior of phonon dispersion and damping across a thermal transition in manganites [17–19]. The inelastic neutron scattering data reveals that phonons broaden and soften considerably as one makes a transition from a ferromagnetically ordered, homogeneous ground state to a paramagnetic insulator with short-range correlated small polarons. In the insulating state, reduction of states near the Fermi level again causes a decrease in both the softening and damping. While there are additional magnetic degrees of freedom which are relevant in these materials, we believe our framework can be generalized to give a theoretical explanation of these data. Part of our ongoing work is to compute phonon properties using the Langevin equation on the doped Holstein model, to avoid charge ordering physics. If one couples the conduction electrons in this to 'local moments' with a double exchange coupling, the resulting system is a reasonable model for doped manganites. We plan to study the phonon dynamics there.

E. Future problems

1. Going beyond thermal noise

The present paper is based on numerical calculations done with a white, memoryless noise field. While this may be a good enough approximation for $\omega \ll k_B T$, to estimate the low T behavior, one has to include memory effects encoded within $[\Pi]^K_{ij}(\omega)$. This is easier said than done, but the lowest order modification will be to introduce a 'thermal correlation time' that goes to zero in the high T limit. This will also

make the damping term nonlocal in time with the same τ_{th} timescale. The calculation of such a characteristic time has to be done by calculating the polarizability in the adiabatic approximation. This extension of the present scheme will give rise to an equation which is more complicated to solve numerically but contains more quantum fluctuation effects which are important when $k_BT \ll \omega$.

2. Acoustic phonons, multiple atomic species

The present study contains a single optical phonon mode coupled to conduction electrons. To model a more realistic physical system, one has to include additional vibrational modes like acoustic phonons. This requires a term with intersite couplings at the noninteracting level. One may readily introduce such terms in the instantaneous Hamiltonian of the present scheme. Moreover, multiple atomic species with different masses can be also brought in within the same basic equation. This amounts to just changing the inertia term and has a bearing on the phonon scattering rates.

3. Impact of disorder

Real materials like manganites always have intrinsic disorder effects arising from a substitutional origin. One may introduce potential disorder in the present scheme directly through the Hamiltonian. Moreover, one can also put in random mass terms (taken from a binary distribution) to mimic a disordered medium. The main effect should be on the phonon damping, which will increase substantially even at low temperature. Disorder will also suppress quantum tunneling effects making our strategy more justifiable at low enough temperatures.

VI. CONCLUSIONS

We have studied the real time dynamics of the Holstein model at half filling using a Langevin approach. This exploits the smallness of the bare phonon energy with respect to the electron hopping to simplify the 'force' acting on the phonon degrees of freedom. Using exact diagonalization of the electron problem and Newtonian evolution of the stochastic equation we establish the phonon dynamics from the low temperature charge ordered phase, through the critical region, into the high temperature polaron liquid phase. This reveals nonmonotonic variation in both the mean energy $\omega_{\mathbf{q}}$ and damping $\Gamma_{\mathbf{q}}$ of the phonon modes with respect to temperature. This approach, building in large amplitude dynamical fluctuations, can help address a wide variety of finite temperature phonon problems including issues of thermal transport. Using an auxiliary field approach it can also approach the dynamics of other correlated electron problems.

ACKNOWLEDGMENTS

We acknowledge use of the High Performance Computing Facility at HRI. The research was supported in part by an Infosys scholarship for senior students.

[1] J. M. Ziman, *Electrons and phonons* (Oxford University Press, Oxford, 2001).
[2] J. Bardeen, L. N. Cooper, and J. R. Schrieffer, Phys. Rev. **108**, 1175 (1957).
[3] G. Gruner, Rev. Mod. Phys. **60**, 1129 (1988).
[4] D. Emin, *Polarons* (Cambridge University Press, Cambridge, 2012).
[5] A. S. Alexandrov, *Polarons in Advanced Materials* (Springer, Dordrecht, The Netherlands, 2007).
[6] Y. Tokura, Phys. Today **56**(7), 50 (2003).
[7] M. Imada, A. Fujimori, and Y. Tokura, Rev. Mod. Phys. **70**, 1039 (1998).
[8] Y. Tokura, *Colossal Magnetoresistive Oxides* (CRC Press, London, 2000).
[9] A. S. Alexandrov and N. F. Mott, *Polarons and Bipolarons* (World Scientific, Singapore, 1995).
[10] S. Blawid and A. J. Millis, Phys. Rev. B **63**, 115114 (2001).
[11] S. W. Lovesey (ed.), *Dynamics of Solids and Liquids by Neutron Scattering* (Springer-Verlag, Berlin, Heidelberg, 1977).
[12] N. Mannella, W. L. Yang, X. J. Zhou, H. Zheng, J. F. Mitchell, J. Zaanen, T. P. Devereaux, N. Nagaosa, Z. Hussain, and Z.-X. Shen, Nature (London) **438**, 474 (2005).
[13] M. Sentef, A. F. Kemper, B. Moritz, J. K. Freericks, Z.-X. Shen, and T. P. Devereaux, Phys. Rev. X **3**, 041033 (2013).
[14] P. Bruesch, *Phonons: Theory and Experiments* (Springer-Verlag, Berlin, Heidelberg, 1982), Vol. I–III.
[15] R. Blankenbecler, D. J. Scalapino, and R. L. Sugar, Phys. Rev. D **24**, 2278 (1981).
[16] A. Georges, G. Koliar, W. Krauth, and M. J. Rozenberg, Rev. Mod. Phys. **68**, 13 (1996).
[17] F. Weber, N. Aliouane, H. Zheng, J. F. Mitchell, D. N. Argyriou, and D. Reznik, Nat. Mater. **8**, 798 (2009).
[18] F. Weber, S. Rosenkranz, J.-P. Castellan, R. Osborn, H. Zheng, J. F. Mitchell, Y. Chen, S. Chi, J. W. Lynn, and D. Reznik, Phys. Rev. Lett. **107**, 207202 (2011).
[19] M. Maschek, D. Lamago, J.-P. Castellan, A. Bosak, D. Reznik, and F. Weber, Phys. Rev. B **93**, 045112 (2016).
[20] C. E. Creffield, G. Sangiovanni, and M. Capone, Eur. Phys. J. B **44**, 175 (2005).
[21] M. Hohenadler, H. Fehske, and F. F. Assaad, Phys. Rev. B **83**, 115105 (2011).
[22] J. Loos, M. Hohenadler, A. Alvermann, and H. Fehske, J. Phys.: Condens. Matter **18**, 7299 (2006).
[23] D. Meyer, A. C. Hewson, and R. Bulla, Phys. Rev. Lett. **89**, 196401 (2002).
[24] S. Blawid, A. Deppeler, and A. J. Millis, Phys. Rev. B **67**, 165105 (2003).
[25] S. Sykora, A. Hübsch, K. W. Becker, G. Wellein, and H. Fehske, Phys. Rev. B **71**, 045112 (2005).
[26] S. Sykora, A. Hübsch, and K. W. Becker, Europhys. Lett. **76**, 644 (2006).
[27] M. Weber, F. F. Assaad, and M. Hohenadler, Phys. Rev. B **91**, 235150 (2015).

[28] A. Kamenev, *Field Theory of Non-Equilibrium Systems* (Cambridge University Press, Cambridge, 2011).
[29] D. Mozyrsky, M. B. Hastings, and I. Martin, Phys. Rev. B **73**, 035104 (2006).
[30] A. Zazunov and R. Egger, Phys. Rev. B **81**, 014508 (2010).
[31] J.-T. Lu, M. Brandbyge, P. Hedegard, T. N. Todorov, and D. Dundas, Phys. Rev. B **85**, 245444 (2012).
[32] P. C. Hohenberg and B. I. Halperin, Rev. Mod. Phys. **49**, 435 (1977).
[33] G.-W. Chern, K. Barros, Z. Wang, H. Suwa, and C. D. Batista, Phys. Rev. B **97**, 035120 (2018).
[34] S. Bhattacharyya, S. Pradhan, and P. Majumdar, arXiv:1711.08749.
[35] L. Kades and J. M. Pawlowski, arXiv:1901.05214.